Materials Advances

ROYAL SOCIETY OF CHEMISTRY

PAPER

View Article Online
View Journal | View Issue

Cite this: *Mater. Adv.*, 2024, 5, 7035

Synergistic antibacterial effect of quaternary ammonium salt functionalized metal–organic framework†

Ming Zhou, [ab] Bin Zhang,[a] Tan Wang,[a] Ping Xiao,[a] Lin Cheng[a] and Rui Tang*[c]

Received 13th May 2024,
Accepted 29th July 2024

DOI: 10.1039/d4ma00496e

rsc.li/materials-advances

Pseudomonas aeruginosa (*P. aeruginosa*) can be an important causative factor for severe infections in humans, especially in patients with respiratory infections. Herein, we have designed a quaternary ammonium salt (QAS)-functionalized metal–organic framework (MOF) material, which combines the physical antibacterial and photodynamic therapeutic properties of nanomaterials to achieve high antibacterial efficiency. It is worth noting that positively charged nanomaterials can effectively adhere to the surface of bacteria, destroying the structure of the cell membrane, and then cooperating with the free radicals released by light irradiation to achieve a more thorough antibacterial effect. The antibacterial activity of the nanomaterials against *P. aeruginosa* was over 90% within 20 minutes. Therefore, MOF materials modified with QAS have enormous effective potential in antimicrobial applications.

1. Introduction

Infections caused by bacteria pose a serious threat to human health across the globe, inducing multiple diseases and complications.[1,2] Currently, antibiotics are generally a widely used strategy for combating pathogenic bacteria. However, after long-term abuse of antibiotics, the emergence of drug-resistant bacteria has become a new challenging threat to current anti-infective therapies.[3–6] Therefore, it is urgent to research effective antibacterial methods to eradicate bacteria. The initial step in modern detection and treatment processes towards cancer/pathogens is to allow therapeutic agents to enter target cells, which is the premise of therapeutic functions.[7–9] To enhance and stabilize the effects of the developed agents, scientists have involved many organic molecules and biomolecules as targeting agents to help cell entrance, as these exogenous molecules have strong and specific affinity to cells/pathogens.[10–13]

Recently, photodynamic therapy (PDT) and photothermal therapy (PTT) have attracted great attention due to their ability to accurately produce a desired therapeutic effect upon laser activation; therefore the side effects and drug resistance associated with conventional chemotherapy are minimized.[14,15] Moreover, PDT and PTT have also been used in concert to achieve disease theranostics based on the inherent fluorescence of photosensitizers (*i.e.* chemical agents that exhibit PDT/PTT effects).[16–18] However, an exploration of PDT/PTT combined with highly efficient antibacterial therapy has always been a severe challenge. Porphyrin has been developed as an effective PDT agent that would produce singlet oxygen ($^1O_2$) upon 660-nm laser irradiation.[19] Moreover, it has multiple modification sites allowing for subsequent functionalization with nanomaterials.[20,21]

As a type of newly emerging optical/electronic material, metal–organic frameworks (MOFs), which are one of the most multifunctional porous materials constructed from metals and organic ligands, possess the advantages of structural regulation, easy functionalization and good biocompatibility, and they have been identified as suitable scaffolds for many applications, especially in biomedical applications.[22–26] For example, Fe-TBP was constructed from Fe_3O clusters and a 5,10,15,20-tetra(*p*-benzoato)porphyrin (TBP) ligand.[27] Fe-TBP directly incorporates photosensitizers (PSs) as building units, allowing for high PS loadings without self-quenching. The porous structures of Fe-TBP also facilitate the diffusion of reactive oxygen species (ROS), improving the PDT efficacy of Fe-TBP over other nano-photosensitizers (nPSs). Furthermore, Fe-TBP has unsaturated metal sites, and small molecular compounds are used to modify the surface of Fe-TBP through coordination bonds or non-covalent forces, which endows the material with new functions and achieves synergistic antibacterial effects.[28–30]

This study constructed a novel and highly efficient antibacterial nanoplatform for the treatment of bacterial infections by synergistic chemo-photodynamic therapy. The fabrication and

[a] *Department of General Surgery, Shanghai Xuhui District Dahua Hospital, Shanghai, China*
[b] *Department of General Surgery, people's Hospital of Yuanyan Country, Yunnan Province, China*
[c] *Department of Hernia and Abdominal Wall Surgery, East Hospital Affiliated to Tongji University, Shanghai, China. E-mail: kevintown@126.com*

† Electronic supplementary information (ESI) available: Experimental section, additional figures and original spectral copies of new compounds. See DOI: https://doi.org/10.1039/d4ma00496e

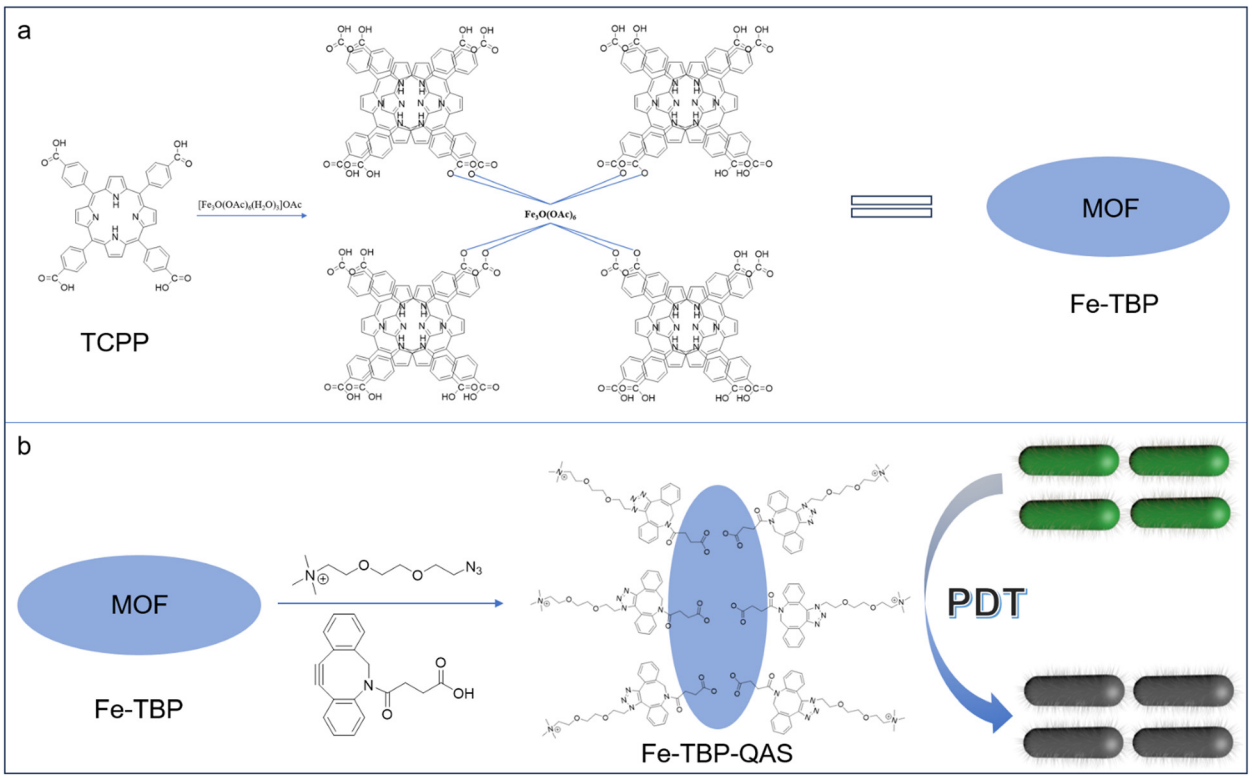

Scheme 1 (a) Construction of Fe-TBP nanomaterials. (b) Self-assembly of **Fe-TBP–QAS** nanomaterials and synergistic photodynamic antibacterial applications.

antibacterial mechanism of MOF nanomaterials are shown in Scheme 1. First, Fe-TBP was synthesized from $[Fe_3O(OAc)_6(H_2O)_3]OAc$ and H_4TBP solvothermally and showed a nanorice morphology. Then, DBCO was anchored to the surface of Fe-TBP through coordination bonding. Finally, quaternary ammonium salt (QAS) molecules were coupled to the surface of Fe-TBP through a strain-promoted alkyne–azide cycloaddition (SPAAC) strategy to obtain **Fe-TBP–QAS** nanomaterials. As a target molecule, QAS is electrostatically adsorbed by negatively charged bacteria.[31,32] This leads to the aggregation of Fe-TBP materials on the cell wall, generating a room-impeding effect that inhibits bacterial growth and causes cell death. In addition, QAS brings the Fe-TBP material closer to the bacteria, reducing the distance of free radical diffusion to the bacteria. This enhancement improves the effectiveness of photodynamic therapy, so a synergistic photodynamic antibacterial effect is achieved.

2. Results and discussion

Fe-TBP–QAS were synthesized using an established procedure. First, the Fe-TBP material was synthesized using *meso*-tetra(4-carboxyphenyl)porphine (TCPP) as the photosensitizer, and then the QAS group was used to modify the the surface of the Fe-TBP material by coordination bonds and strain-promoted alkyne–azide cycloaddition (SPAAC) strategies.

A series of techniques were used for the characterization of the **Fe-TBP–QAS** nanomaterials. Scanning electron microscopy (SEM) was used to characterize the morphology of the constructed **Fe-TBP–QAS**. The Fe-TBP material showed a well-defined ellipsoidal morphology with a uniform size of ~100 nm in the scanning electron microscope (SEM) images. A uniform distribution of N, O, C, and Fe was observed in the Fe-TBP particles by dark-field SEM analysis. The Fe element belongs to the Fe_3O cluster, and the N element belongs to TCPP. Similarly, with a uniform size distribution, an ellipsoidal morphology was seen for **Fe-TBP–QAS**. Due to the modification by the QAS group of the particle surface, observation of the SEM image shows an increase in the surface roughness of **Fe-TBP–QAS** (Fig. 1). From analysis of the hydrokinetic diameter, it is observed that the particle size of the material was slightly increased after the surface modification by the QAS group (Fig. S2a, ESI†). The elemental components and valence states of **Fe-TBP–QAS** were determined by X-ray photoelectron spectroscopy (XPS). The investigated spectra showed that the material contained C, N, O and Fe (Fig. S2b, ESI†), consistent with SEM elemental mapping analysis.

Additionally, Fourier-transform infrared (FT-IR) spectroscopy was used to analyze the synthesized **Fe-TBP–QAS**. First, the absorption peaks of the Fe_3O cluster at 1590 cm^{-1} and 1450 cm^{-1} corresponded to the carboxylate radical, and the absorption peak of Fe_3O was at 610 cm^{-1}. Then, we found that the broad absorption in the range of 2500–3150 cm^{-1} corresponding to the hydroxyl group of COOH of free TCPP disappeared, whereas the absorption peak of the carbonyl group went from 1700 cm^{-1} to two new peaks at 1700 and 1650 cm^{-1}

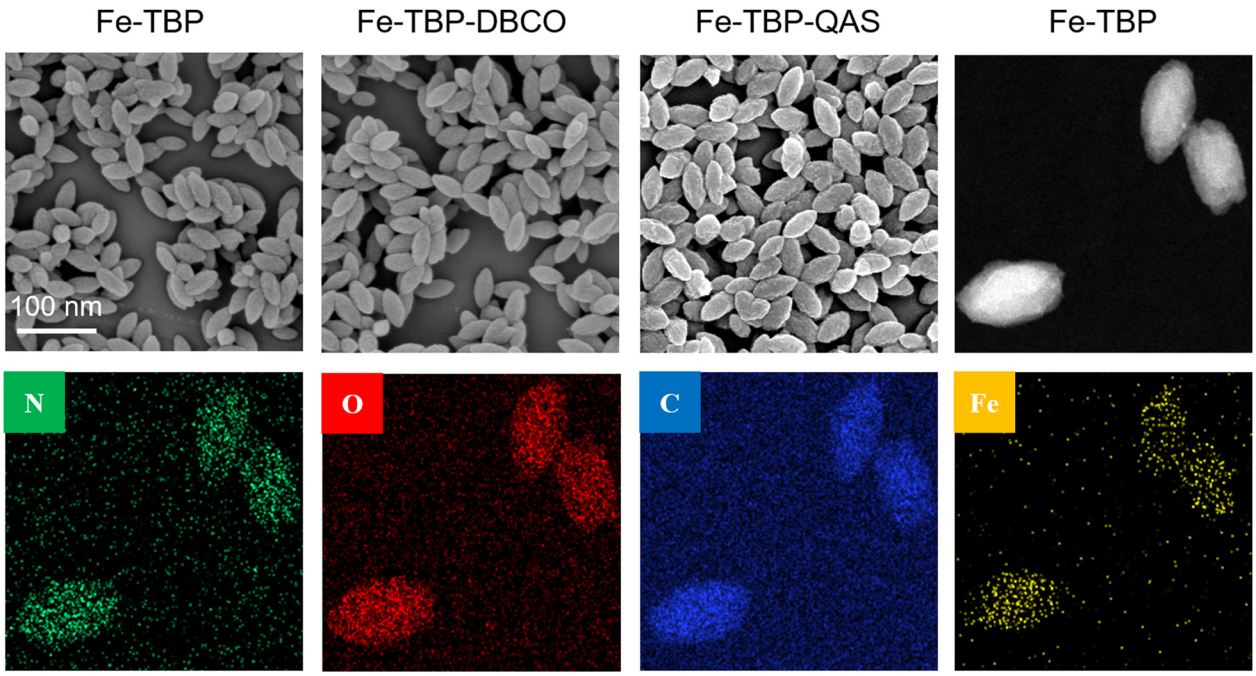

Fig. 1 SEM images of of Fe-TBP, Fe-TBP–DBCO and **Fe-TBP–QAS** nanomaterials and dark-field scanning transmission electron microscopy image and elemental maps of Fe-TBP nanomaterials.

(Fig. S1a, ESI†). These results indicated the formation of ionic bonds between the Fe_3O cluster and COO^-, consistent with data in previous reports. The N–H stretching vibration of TCPP at 965 cm^{-1} remained, suggesting that iron ions were not coordinated in the porphyrin center of TCPP except as metal nodes. Then, the efficient anchoring of the DBCO group onto Fe-MLM was confirmed by the appearance of a band at 2250–2100 cm^{-1} assigned to the carbon–carbon triple bond. After the QAS group was coupled by an alkyne–azide cycloaddition reaction, the characteristic peaks of the carbon–carbon triple bond disappeared. Moreover, the absorption bands at around 1103 and 2850 cm^{-1} were attributed to C–O–C and $-CH_2$ vibration from the Fe-MLM surface QAS group (Fig. S1b, ESI†). UV-vis techniques were also used to characterize TCPP, Fe-TBP, and **Fe-TBP–QAS** (Fig. S2c, ESI†). In the UV-vis spectrum of Fe-TBP, the main peak could be observed at 415 nm, and four weak Q bands at 515 nm, 550 nm, 590 nm and 645 nm, characteristic of TCPP, were visible. Compared with TCPP, the main UV absorption peak of Fe-TBP shows a slight red shift. Meanwhile, powder X-ray diffraction (PXRD) tests also confirmed that the prepared Fe-TBP material structure matched that of Fe-TBP predicted by simulation (Fig. S3, ESI†), indicating the successful construction of Fe-TBP MOF materials. In the UV-vis spectrum of **Fe-TBP–QAS**, the absorption peak at 310 nm is attributed to the DBCO group, indicating that DBCO molecules were successfully anchored onto the surface of Fe-TBP. The zeta potentials of Fe-TBP and Fe-TBP–DBCO were −14.0 and −10.1 mV, respectively, while that of **Fe-TBP–QAS** was about 7.9 mV (Fig. S2d, ESI†). These phenomena indicate that QAS successfully modified the surface of the Fe-TBP MOF material.

Next, N_2 adsorption–desorption measurements were employed to analyze the specific surface area of **Fe-TBP–QAS**. The BET specific surface area (SBET) of **Fe-TBP–QAS** is 321.9296 $m^2\ g^{-1}$ (Fig. 2a). The photodynamic activity of **Fe-TBP–QAS** was evaluated to explore potential biomedical applications. The types of free radicals produced by the **Fe-TBP–QAS** materials were evaluated by electron spin resonance (ESR) spectroscopy experiments. We used 5,5-dimethyl-1-pyrroline-*N*-oxide (DMPO) as a trapping agent for $^{\bullet}OH$. The results showed a quadruple signal with relative strength 1 : 2 : 2 : 1, which is characteristic of DMPO–OH species (Fig. 2b).

Morphological changes in *P. aeruginosa* treated with different materials were observed by SEM (Fig. 3). Initially, a rod-like morphology was observed in the SEM images of *P. aeruginosa*. The morphology of the bacteria did not change after 650-nm light (1 W cm^{-2}, 650 nm) irradiation in the absence of the nanomaterials. Then, the morphology of the bacteria also significantly changed in the presence of Fe-TBP with light illumination. After 20 minutes of light illumination, the morphology of the bacteria could be observed to show obvious

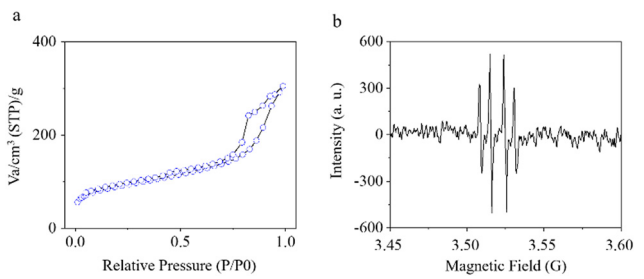

Fig. 2 (a) Nitrogen adsorption isotherms of **Fe-TBP–QAS**. (b) ESR spectra for the measurement of reactive oxygen species ($^{\bullet}OH$) with DMPO upon irradiation of **Fe-TBP–QAS** with 650-nm light (1 W cm^{-2}) for 20 min.

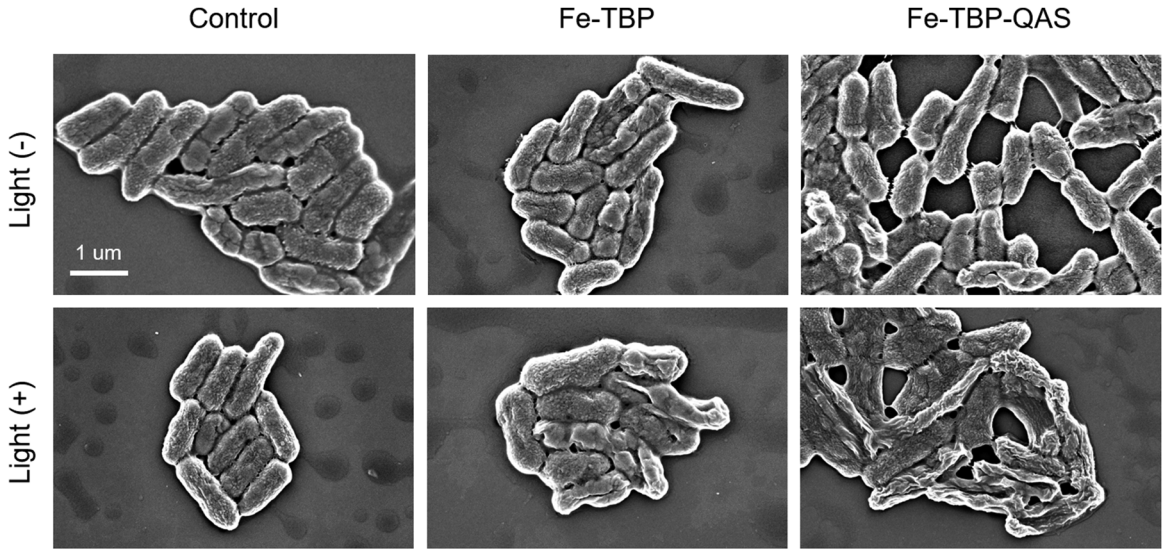

Fig. 3 SEM analysis of *P. aeruginosa* before and after treatment with Fe-TBP and **Fe-TBP–QAS** in the absence and presence of 650-nm light irradiation.

folds. Interestingly, in the presence of **Fe-TBP–QAS** with light illumination for 20 minutes, there was a more pronounced morphological change on the bacteria surface, in which could be found evident depressions and more folds in the bacterial morphology. This suggests that the synergistic therapy strategy can effectively enhance the antibacterial effect.

Finally, the bacteriostatic properties of the nanomaterials were evaluated to analyze their potential clinical applications. We first evaluated the minimum inhibitory concentration (MIC) and minimum bactericidal concentration (MBC) of **Fe-TBP–QAS** for *P. aeruginosa* (ATCC 27853) and methicillin-resistant *Staphylococcus aureus* (MRSA, ATCC 43300) (Table 1). Then, the antibacterial efficiency of the nanomaterials was evaluated by the plate counting method. In the control group, the inhibition performance of *P. aeruginosa* was negligible either under laser irradiation or without laser irradiation. However, a higher inhibition performance toward *P. aeruginosa* was found with Fe-TBP, as 200 μg mL^{-1} Fe-TBP could kill nearly 42% under 650-nm irradiation (1 W cm^{-2}) for 20 min, but less than 10% without laser irradiation. Interestingly, **Fe-TBP–QAS** shows better inhibition performance based on the synergistic inhibition properties of quaternary ammonium salt groups and photodynamic therapy, killing nearly 90% of *P. aeruginosa*. Meanwhile, we also evaluated the antibacterial effect of the Fe-TBP and **Fe-TBP–QAS** materials against MRSA under the same experimental conditions, and the results showed that the Fe-TBP materials modified by quaternary ammonium salts showed a better broad-spectrum antibacterial effect (Fig. 4a and Fig. S4b, ESI†).

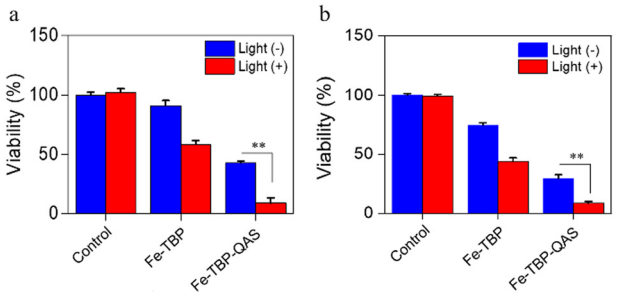

Fig. 4 Viability of *P. aeruginosa* (a) and MRSA (b) treatment with Fe-TBP and **Fe-TBP–QAS** in the absence and presence of 650-nm light irradiation. $^{**}P < 0.01$.

Table 1 Minimum inhibitory concentration (MIC) and Minimum bactericidal concentration (MBC) of the **Fe-TBP–QAS** for *P. aeruginosa* and MRSA

	P. aeruginosa (ATCC 27853)		MRSA (ATCC 43300)	
Sample	MIC (μg mL^{-1})	MBC (μg mL^{-1})	MIC (μg mL^{-1})	MBC (μg mL^{-1})
Fe-TBP–QAS	512	1024	512	1024

3. Conclusions

In summary, we have described the modification by a QAS group of the surface of Fe-TBP materials by coordination bonds and a strain-promoted alkyne–azide cycloaddition strategy, and its antimicrobial studies. The results show that **Fe-TBP–QAS** has good antibacterial activity, which is attributed mainly to the synergistic effect of the physical bacteriostasis of the QAS group and the photodynamic therapy properties of porphyrin molecules. Interestingly, QAS group modification imparted negative charge properties to the surface of the nanomaterials, which effectively improved the affinity between the nanomaterials and the bacteria, and significantly improved the photodynamic therapy performance, which then cooperated with the physical destruction of cell membrane properties by the QAS group to achieve a more thorough antibacterial effect. Our strategy provides an effective antimicrobial therapy for the treatment of *P. aeruginosa* infection, which also provides a potential

reference value for the use of promising antimicrobial nanomaterials in the fight against antimicrobial resistance.

Data availability

The data supporting this article have been included as part of the ESI.†

Conflicts of interest

The authors declare no conflict of interest.

Acknowledgements

The authors thank the Shanghai Xuhui District Medical Research Project (SHXH202101).

Notes and references

1 N. Woodford and D. M. Livermore, *J. Infect.*, 2009, **59**, S4–S16.
2 S. A. Yavari, S. M. Castenmiller, J. A. G. Strijp and M. Croes, *Adv. Mater.*, 2020, **32**, 2002962–2002986.
3 C. J. L. Mrray, K. S. Ikuta and F. Sharara, *et al.*, *Lancet*, 2022, **399**, 629–655.
4 R. U. Chmiel, A. Marek, D. S. Pyśniak, K. Wieczorek, M. Dec, A. Nowaczek and J. Osek, *Antibiotics*, 2022, **11**, 1079–1118.
5 D. C. Nwobodo, M. C. Ugwu, C. O. Anie, M. T. S. Al-Ouqaili, J. C. Ikem, U. V. Chigozie and M. Saki, *J. Clin. Lab. Anal.*, 2022, **36**, 24655–24664.
6 F. Akram, M. Imtiaz and I. Haq, *Microb. Pathog.*, 2023, **174**, 105923.
7 J. M. V. Makabenta, A. Nabawy, C. H. Li, S. S. Malan, R. Patel and V. M. Rotello, *Nat. Rev. Microbiol.*, 2021, **19**, 23–36.
8 H. Y. Min and H. Y. Lee, *Exp. Mol. Med.*, 2022, **54**, 1670–1694.
9 Y. Yang, B. Chu, J. Cheng, J. Tang, B. Song, H. Wang and Y. He, *Nat. Commun.*, 2022, **13**, 1255–1269.
10 D. Han, X. Liu and S. Wu, *Chem. Soc. Rev.*, 2022, **51**, 7138–7169.
11 Y. M. Zuo, X. Yan, J. Xue, L. Y. Guo, W. W. Fang, T. C. Sun, M. Li, Z. Zha, Q. Yu, Y. Wang, M. Zhang, Y. Lu, B. Cao and T. He, *ACS Appl. Mater. Interfaces*, 2020, **12**, 4333–4342.
12 Z. Geng, Z. Cao and J. Liu, *Exploration.*, 2023, **3**, 20210117.
13 C. Deusenbery, Y. Wang and A. Shukla, *ACS Infect. Dis.*, 2021, **7**, 695–720.
14 Y. Chen, Y. Gao, Y. Chen, L. Liu, A. Mo and Q. Peng, *J. Controlled Release*, 2020, **328**, 251–262.
15 X. Hu, H. Zhang, Y. Wang, B. C. Shiu, J. H. Lin, S. Zhang, C. W. Lou and T. T. Li, *Chem. Eng. J.*, 2022, **450**, 138129.
16 H. Kim, Y. R. Lee, H. Jeong, J. Lee, X. Wu, H. Li and J. Yoon, *Smart Molecules*, 2023, **1**, 20220010.
17 Z. Yan, D. Wang and Y. Gao, *Front. Bioeng. Biotechnol.*, 2023, **11**, 1192960.
18 D. X. Liu, H. Liu, J. Zhang, Y. Hao, H. Yang, W. Zhao and C. Mao, *Biomater. Sci.*, 2022, **10**, 5608–5619.
19 J. Oyim, C. A. Omolo and E. K. Amuhaya, *Front. Chem.*, 2021, **9**, 635344.
20 N. Rabiee, M. T. Yaraki, S. M. Garakani, S. M. Garakani, S. Ahmadi, A. Lajevardi, M. Bagherzadeh, M. Rabiee, L. Tayebi, M. Tahriri and M. R. Hamblin, *Biomaterials*, 2020, **232**, 119707.
21 C. J. P. Monteiro, M. A. F. Faustino and C. Serpa, *Molecules*, 2023, **28**, 7108–7113.
22 J. Yang and Y. W. Yang, *Small*, 2020, **16**, 1906846.
23 A. Wang, M. Walden, R. Ettlinger, F. Kiessling, J. J. Gassensmith, T. Lammers, S. Wuttke and Q. Peña, *Adv. Funct. Mater.*, 2023, 2308589.
24 C. Wang, X. Jia, W. Zhen, M. Zhang and X. Jiang, *ACS Biomater. Sci. Eng.*, 2019, **5**, 4435–4441.
25 P. Cao, X. Wu, W. Zhang, L. Zhao, W. Sun and Z. Tang, *Ind. Eng. Chem. Res.*, 2020, **59**, 1559–1567.
26 P. Li, J. Li, X. Feng, J. Li, Y. Hao, J. Zhang, H. Wang, A. Yin, J. Zhou, X. Ma and B. Wang, *Nat. Commun.*, 2019, **10**, 2177–2186.
27 G. Lan, K. Ni, Z. Xu, S. S. Veroneau, Y. Song and W. Lin, *J. Am. Chem. Soc.*, 2018, **140**, 5670–5673.
28 M. He, T. Yang, Y. Wang, M. Wang, X. Chen, D. Ding, Y. Zheng and H. Chen, *Adv. Healthcare Mater.*, 2021, **10**, 2002104.
29 G. Lan, K. Ni, Z. Xu, S. S. Veroneau, Y. Song and W. Lin, *J. Am. Chem. Soc.*, 2018, **140**, 5670–5673.
30 Y. Luo, J. Li, X. Liu, L. Tan, Z. Cui, X. Feng, X. Yang, Y. Liang, Z. Li, S. Zhu, Y. Zheng, K. W. K. Yeung, C. Yang, X. Wang and S. Wu, *ACS Cent. Sci.*, 2019, **5**, 1591–1601.
31 H. Kono, Y. Sogame, U. E. Purevdorj, M. Ogata and K. Tajima, *ACS Appl. Nano Mater.*, 2023, **6**, 4854–4863.
32 Y. Huang, S. Huo, J. Mo and D. Huang, *ACS Omega*, 2023, **8**, 34687–34697.